Frequency Division Based Coordinated Control of Three-Port Converter Interfaced Hybrid Energy Storage Systems in Autonomous DC Microgrids

PANBAO WANG[1], **(Member, IEEE), XIAONAN LU**[2], **(Member, IEEE),**
WEI WANG[1]**, (Member, IEEE), AND DIANGUO XU**[1]**, (Fellow, IEEE)**
[1]Electrical Engineering Department, Harbin Institute of Technology, Harbin 150001 China
[2]Energy Systems Division, Argonne National Laboratory, Lemont, IL 60439, USA

Corresponding author: Panbao Wang (wangpanbao@hit.edu.cn)

ABSTRACT DC microgrids (MGs) feature remarkable advantages of integrating renewable energy sources and loads with DC coupling. In order to improve the operation performance of a dc MG in both steady and transient states, in this paper a hybrid energy storage system (HESS) interfaced by a three-port converter (TPC) is studied. Particularly, a battery and an ultra-capacitor (UC), which form the HESS, are connected at the source side of the TPC, respectively. Aiming at a phase-shifting controlled full-bridge isolated TPC, in addition to conventional droop control loop, a frequency division-based control method is proposed to achieve rational power sharing between the battery and UC. Due to the characteristics of TPC, virtual inductance and virtual capacitance loops are implemented using the input currents at the battery and UC ports. The frequency division between the battery and UC in the HESS is quantitatively analyzed by using the frequency domain small-signal analysis considering the characteristics of power exchange in the phase-shifting controlled TPC. A simulation model built in MATLAB/Simulink and a prototype comprised of a battery, a UC, a programmable dc load, and auxiliary components are implemented to validate the proposed TPC-interfaced HESS under different operation scenarios.

INDEX TERMS DC microgrids, droop control, hybrid energy storage system (HESS), three-port converter, virtual impedance.

I. INTRODUCTION

The proliferation of electricity demand and the increasing requirements of renewable power generation urge the evolution of existing energy structure. In order to meet these requirements, renewable energy sources (RESs) have been widely deployed in modern electric grids to support conventional generation mix considering their sustainable nature and relatively low environmental impacts [1], [2]. Microgrids (MGs) as effective solution of integrating various types of RESs and loads have been extensively studied since it was first proposed in 2002 [3]. Since most of the existing power transmission and distribution systems are implemented based on alternative-current (AC) electricity, AC MGs have become the most common type of MGs nowadays [4], [5]. However, direct-current (DC) MGs have drawn increasing attention in the past years due to their significant advantages of high energy conversion efficiency, absence of harmonics

and reactive power, simple algorithm for resynchronization, etc. [6]–[9].

Although AC or DC MGs have numerous advantages, the intermittency of RESs in a MG should be still noticed. In order to tackle the obstacles induced by the intermittent nature of RESs and mitigate the impacts of load variations, energy storage systems (ESSs) are frequently used [10]–[13]. Since different types of energy storage units (ESUs) have diverse characteristics, they have been usually combined as a hybrid ESS (HESS) to cope with the variations in both steady and transient states [14]. A HESS has been widely deployed in various applications, e.g., electric vehicles (EVs), MGs, uninterruptable power supplies (UPSs) and among others [15]–[19]. In [20], a comparative study of the power and energy density of different storages including fuel cells, ultra-capacitors (UCs), and various types of batteries, e.g., valve regulated lead batteries, NiCd batteries, Lithium batteries,

aluminum-electrolytic batteries, etc., are conducted to characterize the advantages of HESS.

Due to different characteristics of ESUs, the appropriate power sharing is a critical issue for operating a HESS. The existing power sharing schemes among different types of ESUs in the HESS can be implemented by using various approaches [21]. Among them, the most frequently used method in MGs is realized based on digital filters. In [22], the power fluctuations induced by wind turbines is extracted using a high pass filter (HPF), and then a compensation term is calculated and the corresponding control command is sent to the UC converter. The remaining power mismatch is then compensated by the batteries. In [23], a HESS and the corresponding coordinated control strategy are proposed and applied in a MG. The fast Fourier transform is employed to decompose the low- and high-frequency power components of fluctuant loads. The drawback of using preceding methods to separate the mismatched power is that it is realized based on the known real-time reference power. However, the MGs are usually run in autonomous operation mode, especially in islanded operation. In this case, it is hard to know the exact power mismatch between droop-controlled components, and the required power of each unit in the HESS is thereby difficult to track.

To solve the above problems, in [24] and [25], a frequency-division method for inverse-droop control with HESS is implemented in voltage-control based power coordination. Additionally, a frequency-coordinating virtual impedance based autonomous power management of DC MGs is proposed in [26]. With the effective shaping of the virtual output impedances in the frequency domain, the battery and UC converters are designed to absorb low-frequency and high-frequency power fluctuations respectively. In [27], by using extra virtual impedance loop, a virtual resistor and a virtual capacitor connected in series are added between the converter and dc bus. The UC in the HESS can provide surge current compensation via its interface converter and the proposed control scheme. In [28], an integral droop control is proposed for transient power allocation and output impedance shaping of HESS in DC MGs in a decentralized manner. In [29], a control strategy consisting of a HPF-based droop controller for battery converter and a virtual capacitance droop controller for UC converter is proposed. Dynamic power sharing, bus voltage restoration, and UC SoC recovery are achieved without communications.

Meanwhile, multiport converter topologies was proposed and used in the interface converters [30]–[32]. A non-isolated buck/boost-converter-based three-port converter (TPC) is proposed in [33]. Since only a single energy conversion stage is needed in the TPC, the advantages of high power density and high energy conversion efficiency can be realized. The topologies of the existing TPCs, e.g., half-bridge, full-bridge, boost half-bridge and boost full-bridge, etc., and the corresponding operation principles are investigated in [34]. Meanwhile, an isolated three-phase TPC with common DC bus is studied. Compared to traditional buck/boost converters,

isolated multi-port converters feature the characteristics of high voltage conversion ratio, and electrical isolation, etc. In addition, by using phase-shifting control [35], the soft switching in multi-port converters with a full-bridge configuration is easy to be achieved [36].

In order to integrate HESS into DC MGs efficiently and realize reasonable power sharing, in this paper, a full-bridge isolated TPC is employed as the interface of the HESS in a DC MG. The equivalent circuit model and phase-shifting control of this type TPC are discussed. Focusing on autonomous operation modes and the characteristics of a TPC, an adaptive power sharing method based on virtual inductance and virtual capacitance is proposed. By emulating the physical characteristics of an inductor and a capacitor, the mismatched power between sources and loads in a DC MG can be automatically separated based on different frequency characteristics, i.e., the autonomous frequency division power sharing in a TPC can be achieved. Simulation and experimental validations are conducted to verify the effectiveness of the proposed control and energy management methods of HESS.

The rest of the paper is organized as follows. Section II investigates the architecture of DC MGs, and then the topology of full-bridge isolated TPC, which is used in this paper, is presented. Section III presents the model and operation principle of the TPC, and details the frequency division control method with virtual inductance and capacitance loops. Meanwhile, stability analysis of the proposed control method is conducted. Simulation verifications are presented in Section IV. Section V shows the detailed experimental results obtained from the prototype. Finally, Section VI summarizes the paper and draws the conclusion.
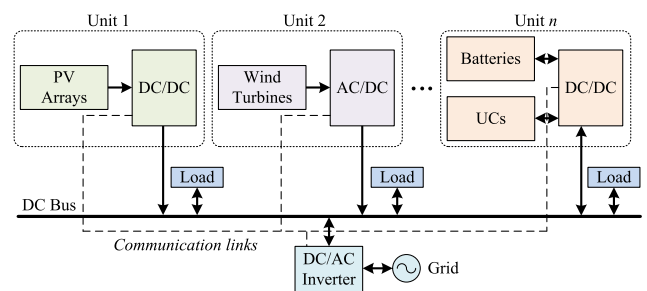

FIGURE 1. Configuration of DC MGs with interconnected HESS.

II. INTERCONNECTION OF THE HESS IN DC MGS

DC MGs are emerging and promising counterparts of conventional AC MGs due to their tremendous advantages [6]. The architecture of a DC MG with HESS is depicted in Fig. 1. As seen in this figure, the DC-DC interface converters of RESs, HESS and local loads are interconnected through the common DC bus. In order to exchange power with the main grid, a bi-directional DC/AC inverter is employed to enable the interactive operation between local DC MG and external AC grids. Meanwhile, in the islanded operation mode, the RESs, HESS and loads are controlled to run in

an autonomous manner. When running in islanded operation mode, the DC bus voltage in DC MG is established and stabilized by the distributed generators (DGs) with non-intermittent power, e.g., ESUs. These non-intermittent and dispatchable DGs are commonly run in the voltage control mode [8]. Usually, droop control is employed in DC MGs to achieve rational power sharing among the voltage-controlled units.

In order to further improve the power density and conversion efficiency of the converters in a HESS, TPCs are employed as the interface converters of HESS in DC MGs. The TPC can exchange power directly between any two ports, and allow the batteries or UCs to interact with the common DC bus directly and independently.

In this study, a phase-shifting controlled full-bridge isolated TPC is employed as the interface of the HESS in a DC MG. The high-voltage port is connected to the DC bus and the two low-voltage ports are connected to batteries and UCs, respectively. The topology of the selected TPC is shown in Fig. 2, which is comprised of three H-bridges and a three-winding HFT.
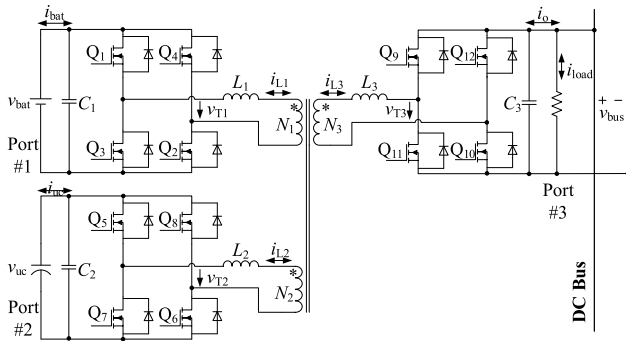

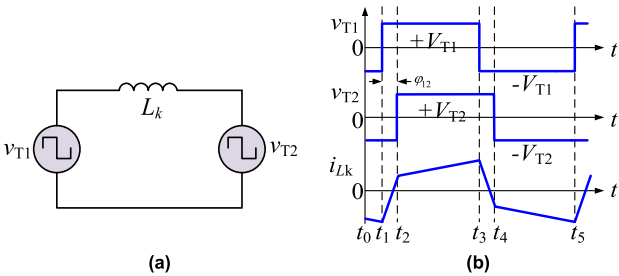**FIGURE 2.** Topology of the full-bridge isolated TPC.

FIGURE 3. Phase-shifting control principle of a two-terminal system.
(a) equivalent circuit model. (b) waveforms of voltage and current.

III. COORDINATED OPERATION OF THE HESS IN TPCS

A. BASIC OPERATION PRINCIPLE OF PHASE-SHIFTING CONTROLLED FULL-BRIDGE TPC

Phase-shifting full-bridge TPC can adjust the power exchange at each port by manipulating the phase-shifting angles. First, a two-terminal system is taken as an example

to introduce how phase-shifting control works. Its equivalent circuit model is shown in Fig. 3 (a), where two symmetrical square waves with equal frequencies and a given phase difference are employed with an inductor L_k linking them. Setting the magnitudes of the left and right square wave voltage sources equal to $\pm V_{T1}$ and $\pm V_{T2}$ respectively, the current and voltage waveforms can be achieved, as shown in Fig. 3(b). By making the phase-shifting angle φ_{12} of the two ports leading or lagging, the bidirectional power flow between the two ports can be easily realized.

The relationship between the power exchange P and the phase-shifting angle φ_{12} between v_{T1} and v_{T2} is expressed as follows [35]:

$$P = \frac{V_{T1}V_{T2}}{\omega L_k}\left(\varphi_{12} - \frac{\varphi_{12}^2}{\pi}\right) \tag{1}$$

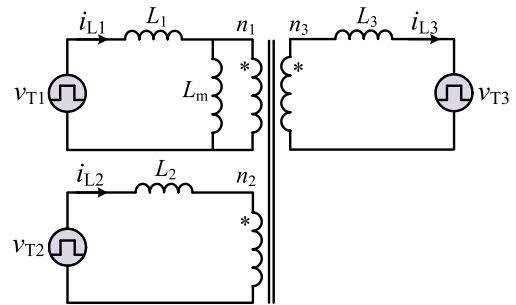where ω is angular frequency ($\omega = 2\pi f$).

FIGURE 4. AC equivalent model of the isolated full-bridge TPC.

Be similar with the phase-shifting control in the two-terminal system, as shown in Fig. 4, the AC equivalent model of the isolated full-bridge TPC can be obtained by replacing the full-bridge under phase-shifting control with three symmetrical square waves. The amplitudes of v_{T1}, v_{T2} and v_{T3} are V_1, V_2 and V_3, and L_m is the equivalent magnetizing inductance of the transformer by converting the total magnetizing inductance of the phase-shifting three-port transformer into port #1.

According to the relationship between the voltage of the three windings of the transformer and the magneto motive balance equation, the following equations can be obtained:

$$\begin{cases} v_{T1} - j\omega_s L_1 i_{L1} = (v_{T2} - j\omega_s L_2 i_{L2}) \cdot \dfrac{n_1}{n_2} \\ v_{T1} - j\omega_s L_1 i_{L1} = (v_{T3} + j\omega_s L_3 i_{L3}) \cdot \dfrac{n_1}{n_3} \\ i_{L1} - i_{Lm} = i_{L3} \cdot \dfrac{n_3}{n_1} - i_{L2} \cdot \dfrac{n_2}{n_1} \end{cases} \tag{2}$$

Further, assuming there is a common point of connection in the TPC, the equivalent model of the transformer can be derived, and the equivalent current and inductance can also be recalculated according to the above equation. The corresponding equivalent model is shown in Fig 5.
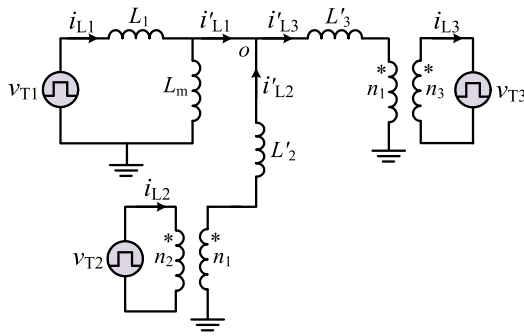
FIGURE 5. Equivalent model of the isolated full-bridge TPC with virtual common point.

B. PROPOSED AUTONOMOUS FREQUENCY DIVISION CONTROL IN HESS

As discussed in Section I, in autonomous DC MGs with HESS, the conventional method based on digital filters cannot separate the power mismatch among hybrid ESUs. In order to solve this issue, an adaptive frequency division based power sharing method based on virtual inductance and virtual capacitance using the input currents at the battery and UC ports is proposed in this subsection.
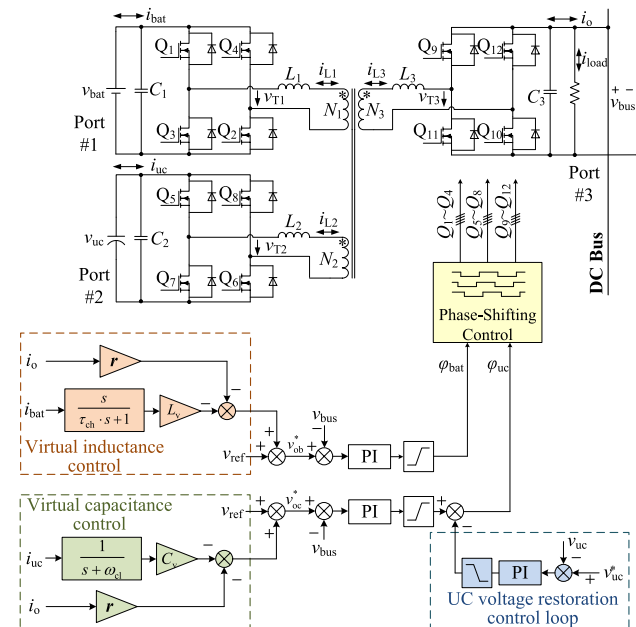

FIGURE 6. Overview control diagram of TPC-interfaced HESS.

The overview figure of the proposed control diagram is shown in Fig. 6, where the proposed virtual inductance control at the battery port is depicted, including constant voltage control loop, conventional droop control loop and virtual inductance control loop.

Since the output power of the battery at the DC bus side of the TPC is hard to be measured, instead of using the secondary current to implement the virtual inductance loop

as in the conventional methods with dedicated converter interfaces for each ESU, the primary current at the battery port, i.e., i_{bat}, is used as the feedback variable, which is sent to the HPF to extract the high-frequency components. Then the HPF output is multiplied by a coefficient L_v and thereby being added to the outer voltage control loop as a negative feedback.

The effect of the proposed virtual inductance can be described as follows. When power or current variations occur, the high-frequency components of the variation can be automatically extracted and added to the outer voltage loop through the HPF, and it plays an important role in removing the high-frequency variations from the output voltage. When the output power or current of the battery is stable, the output value of virtual inductance control loop reduces to 0.

When the proposed virtual inductance control are employed, the reference of the outer voltage control loop can be expressed as:

$$v_{ob}^* = v_{ref} - r \cdot i_o - L_v \cdot \frac{s}{\tau_{ch} \cdot s + 1} \cdot i_{bat} \qquad (3)$$

where v_{ob}^* is the voltage reference generated in the battery converter control diagram; L_v is the virtual inductance; τ_{ch} is the cut-off frequency of the HPF; v_{ref} is the reference voltage at the port #3, i_{bat} is the battery input current at port #1; r is the droop coefficient; v_o and i_o represent the output voltage and output current at port #3; φ_{bat} represents the phase-shifting angle between port #1 and port #3.

The proposed virtual capacitance control at the UC port is also shown in Fig. 6. Similarly to the battery port, in the autonomous operation, a virtual capacitance loop is added in the control diagram of UC converter using the input current at the UC port. The proposed virtual capacitance control is realized by involving a low pass filter (LPF) that uses the input current at the UC port as its input. Multiplying by a coefficient C_v, the output of the virtual capacitance loop is then added into the voltage control loop as a negative feedback. When the DC bus voltage at port #3 is stable, with this embedded virtual capacitance, the output current of UC tends to 0. When RESs or loads variations occur, due to the existence of virtual capacitance, the voltage control loop can compensate the transient power adaptively and rapidly.

By deploying the proposed virtual capacitance control, the reference value of outer voltage control loop v_{oc}^* can be expressed as:

$$v_{oc}^* = v_{ref} - r \cdot i_o - C_v \cdot \frac{1}{s + \omega_{cl}} \cdot i_{uc} \qquad (4)$$

where v_{oc}^* is the voltage reference generated in the UC converter control diagram; C_v is the coefficient of virtual capacitance; ω_{cl} is the cut-off frequency of the LPF; i_{uc} is the UC output current at port #2; φ_{uc} represents the phase-shifting angle between port #2 and port #3 of the TPC.

The equivalent circuit with the proposed inductive and capacitive virtual impedances is shown in Fig. 7, where the UC section is represented using a voltage source connected
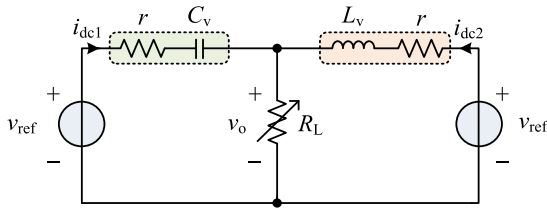
FIGURE 7. Equivalent circuit with the proposed virtual impedance method.

with a capacitor and a resistor in series, and on the other hand, the battery section is shown as a voltage source connected with an inductor and a resistor in series. The HESS is combined of the above sections, which coordinate and supply load dynamics in different frequency ranges.

Additionally, since the terminal voltage of UC can be used to represent the SoC of UC directly, an extra voltage restoration control loop [25] is added into the control diagram of UC port. By setting an average as the reference voltage, the above control loop can ensure the SoC of UC close to 50% of its maximum value in the steady state so that the UC port can flexibly participate in compensating the load variations in both charging and discharging process. The output of the UC voltage restoration control loop is added to the virtual capacitance control, which is reflected in the phase-shifting angle φ_{23}. This additional control loop is employed to restore UC voltage after compensating transient power variations.

C. FREQUENCY DOMAIN ANALYSIS OF TPC-INTERFACED HESS WITH THE AUTONOMOUS FREQUENCY DIVISION CONTROL

In order to quantify the frequency division character-istics considering the phase-shifting control in a TPC, the small-signal model is established to conduct the frequency domain analysis. Particularly, by using phase-shifting control, the power flow among the ports in a TPC can be derived as [37]:

$$P_{13} = \frac{\varphi_{13}(\pi - \varphi_{13})V_1 V_3}{2\pi^2 f_s(L_1 + L_3)} \quad (5)$$

$$P_{23} = \frac{\varphi_{23}(\pi - \varphi_{23})V_2 V_3}{2\pi^2 f_s(L_2 + L_3)} \quad (6)$$

where P_{13} and P_{23} are the power flowing through port #1/#2 to port #3; φ_{13} and φ_{23} are the corresponding phase-shifting angles ($-\pi/2 \le \varphi_{13} \le \pi/2$, $-\pi/2 \le \varphi_{23} \le \pi/2$); V_1, V_2 and V_3 are the equivalent amplitudes of the line frequency voltage components extracted from the input square waves; f_s is the switching frequency of the input square wave; L_1, L_2 and L_3 are the total equivalent inductance at each port.

Let

$$\gamma_{p13} = \frac{V_1 V_3}{2\pi^2 f_s(L_1 + L_3)} \quad (7)$$

$$\gamma_{p23} = \frac{V_2 V_3}{2\pi^2 f_s(L_1 + L_3)} \quad (8)$$

The simplified expression of (5) and (6) can be shown as:

$$P_{13} = \gamma_{p13} \varphi_{13}(\pi - \varphi_{13}) \quad (9)$$

$$P_{23} = \gamma_{p23} \varphi_{23}(\pi - \varphi_{23}) \quad (10)$$

By perturbing the above power flow relationship, the small-signal expression of (9) and (10) can be derived and then transformed into frequency domain, which yields:

$$\hat{p}_{13}(s) = \gamma_{p13}(\pi - 2\Phi_{13}) \cdot \hat{\varphi}_{13}(s) \quad (11)$$

$$\hat{p}_{23}(s) = \gamma_{p23}(\pi - 2\Phi_{23}) \cdot \hat{\varphi}_{23}(s) \quad (12)$$

where Φ_{13} and Φ_{23} are the phase-shifting angles at steady-state operating point; the variables with '^' represent the small-signal variables.

Meanwhile, by considering the control diagram with virtual inductance and virtual capacitance loops, conventional droop control loop and inner voltage and current control loops, it is obtained that:

$$\varphi_{13}(s) = [V_{\text{oref}} - r \cdot i_o(s) - v_o(s)$$
$$- i_{\text{bat}}(s) \cdot G_{\text{lv}}(s)] \cdot G_{\text{piv}}(s)G_{\text{pic}}(s) \quad (13)$$

$$\varphi_{23}(s) = [V_{\text{oref}} - r \cdot i_o(s) - v_o(s)$$
$$- i_{\text{uc}}(s) \cdot G_{\text{cv}}(s)] \cdot G_{\text{piv}}(s)G_{\text{pic}}(s) \quad (14)$$

where $G_{\text{lv}}(s)$ and $G_{\text{cv}}(s)$ are the transfer functions of virtual inductance and capacitance loops; $G_{\text{piv}}(s)$ and $G_{\text{pic}}(s)$ represent the inner voltage and current controllers, respectively.

Hence, the small-signal representations of (13) and (14) are thereby derived as:

$$\hat{\varphi}_{13}(s) = -[r \cdot \hat{i}_o(s) + \hat{v}_o(s) + \hat{i}_{\text{bat}}(s) \cdot G_{\text{lv}}(s)] \cdot G_{\text{piv}}(s)G_{\text{pic}}(s) \quad (15)$$

$$\hat{\varphi}_{23}(s) = -[r \cdot \hat{i}_o(s) + \hat{v}_o(s) + \hat{i}_{\text{uc}}(s) \cdot G_{\text{cv}}(s)] \cdot G_{\text{piv}}(s)G_{\text{pic}}(s) \quad (16)$$

Combining (11) – (12) and (15) – (16) and considering the power balance among three ports, it yields:

$$\hat{p}_o = \hat{p}_{13} + \hat{p}_{23}$$
$$= A \cdot \hat{v}_o(s) + B \cdot \hat{i}_o(s) - C_1 \cdot \hat{i}_{\text{bat}}(s) - C_2 \cdot \hat{i}_{\text{uc}}(s) \quad (17)$$

where

$$A = -[\gamma_{p13}(\pi - 2\Phi_{13}) + \gamma_{p23}(\pi - 2\Phi_{23})] \cdot G_{\text{piv}}(s)G_{\text{pic}}(s)$$
$$B = -r \cdot [\gamma_{p13}(\pi - 2\Phi_{13}) + \gamma_{p23}(\pi - 2\Phi_{23})] \cdot G_{\text{piv}}(s)G_{\text{pic}}(s)$$
$$C_1 = -\gamma_{p13}(\pi - 2\Phi_{13}) \cdot G_{\text{lv}}(s)G_{\text{piv}}(s)G_{\text{pic}}(s)$$
$$C_2 = -\gamma_{p23}(\pi - 2\Phi_{23}) \cdot G_{\text{cv}}(s)G_{\text{piv}}(s)G_{\text{pic}}(s)$$

For the load side at port #3, it is achieved:

$$\begin{cases} v_o = i_o \cdot R_L \\ p_o = v_o \cdot i_o \end{cases} \quad (18)$$

The small-signal representation of (18) in *s* domain can be thereby calculated as:

$$\begin{cases} \hat{v}_o(s) = \hat{i}_o(s) \cdot R_L \\ \hat{p}_o(s) = V_o \cdot \hat{i}_o(s) + I_o \cdot \hat{v}_o(s) \end{cases} \quad (19)$$
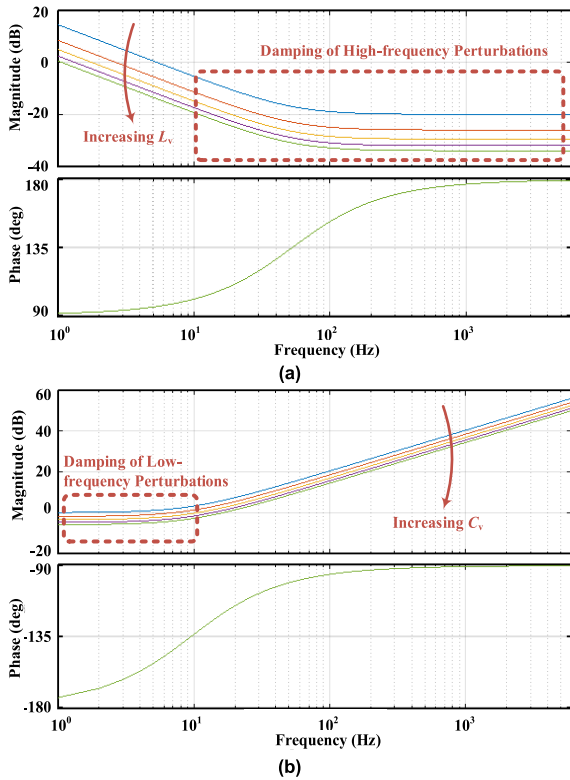
FIGURE 8. Frequency domain analysis results: (a) battery port (G_{bat}) with increasing L_v. (b) UC port (G_{uc}) with increasing C_v.

Combining (17) and (19), it is derived:

$$G_{bat}(s) = \frac{2r \cdot i_o(s) - r \cdot A - B}{2rC_1 \cdot i_o(s)} \tag{20}$$

$$G_{uc}(s) = \frac{2r \cdot i_o(s) - r \cdot A - B}{2rC_2 \cdot i_o(s)} \tag{21}$$

Therefore, the frequency domain characteristics between the battery and UC ports (port #1 and #2) and the output port (port #3) can be shown by using the transfer functions G_{bat} and G_{uc}, respectively.

The corresponding frequency domain analysis results are shown in Fig. 8 (a) and (b) with the system parameters shown in Table 1. Here, φ_{13} and φ_{23} are selected as 30° to show an illustrative operation point. It can be seen that high-frequency perturbations are dampened at the battery port, which means that high-frequency components in the output power at port #3 are blocked at the battery port while compensated at the UC port only. On the other hand, low-frequency perturbations are dampened at the UC port, which means that low-frequency components in the output power at port #3 are blocked at the UC port while only compensated at the battery port.

In order to evaluate the stability of the proposed control diagram, different operation points are tested by exhausting the phase-shifting angles φ_{13} and φ_{23}. In particular, for each φ_{13} within the feasible range, all the feasible φ_{23} with a fixed step change are tested to obtain the set of dominant poles.

TABLE 1. System parameters.

Name	Symbol	Value	Unit
Voltage at port #1	V_1	48	V
Voltage at port #2	V_2	48	V
Voltage at port #3	V_3	320	V
Load resistance	R_L	120	Ω
Total equivalent inductance at port #1	L_1	64	μH
Total equivalent inductance at port #2	L_2	64	μH
Total equivalent inductance at port #3	L_3	83	μH
Switching frequency	f_s	40	kHz
Time constant of the HPF	T_{dh}	3	ms
Cutting frequency of the LPF (angular frequency)	ω_{cl}	377	rad/s
Virtual capacitance	C_v	0.3	F
Virtual inductance	L_v	600	mH
Droop coefficient	r	0.2	Ω

Among these dominant poles, the one with maximum real part (i.e., λ_{max}) is selected and plotted in Fig. 9. Furthermore, by adjusting φ_{13} within its feasible range, all these dominant poles (i.e., λ_{max}) can be derived.
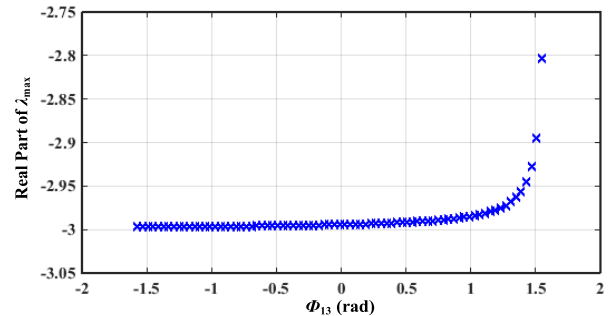

FIGURE 9. Real parts of the dominant poles with exhausted phase-shifting angles.

As shown in Fig. 9, by exhausting the phase-shifting angles, the real parts of all the dominant poles are less than zero, which means that the system stability can be guaranteed.

IV. SIMULATION TESTS

In order to validate the autonomous frequency-division control in TPC-interfaced HESS, a simulation model is implemented in MATLAB/Simulink. As shown in Table 1, the input voltage levels of the battery port and UC port are both 48 V and the load side voltage level at port #3 is 320 V. Meanwhile, the turning ratio of the multi-winding transformer is 3:3:20.

A. CASE I: LOAD INCREASING/DECREASING

As shown in Fig. 10, when the load power increasing or decreasing with changing load resistance, it can be seen that the UC is responsible for absorbing the transient power during load step-up or step-down, while in the steady state,
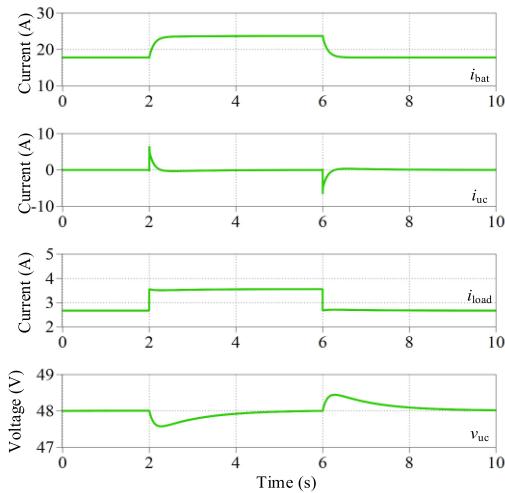
FIGURE 10. Simulation scenario #1: load power increasing and decreasing.

the load power is supplied by the battery. Meanwhile, it should be also noted that the terminal voltage of the UC decreases or increases when compensating the transient power. However, this voltage changes at the UC port can be gradually eliminated by using the additional voltage restoration control loop.

B. CASE II: LOAD CHANGE WITH POWER FLOW REVERSAL
When power flow reversal is triggered by continuous load decreasing or increasing, the operation mode of the battery at port #1 is switched between charging and discharging and the UC at port #2 is still responsible for compensating the transient power. As shown in Fig. 11 (a), the load power keeps decreasing from $t = 2$ s to 4 s. At t = 3.5 s, a power flow reversal is triggered by the decreasing load power. Therefore, the battery is switched from discharging to charging mode. As shown in Fig. 11 (b), when the load power at the port #3 keeps increasing, which even triggers power flow reversal, the battery at port #1 can still effectively provide the steady-state load power with the proposed control method. Meanwhile, the UC at the port #2 is responsible for compensating the transient power.

By combining the results in Fig. 11 (a) and (b), it can be clearly seen that the rational power sharing in the TPC-interfaced HESS is realized by using the frequency division control with bidirectional power flow. Meanwhile, smooth transition between charging and discharging modes can be also implemented without specifying the reference power exchange since the proposed TPC-interfaced HESS system is operated in autonomous operation mode.

C. CASE III: LOAD CURRENT RIPPLE SEPARATION
Since virtual inductance and capacitance are employed in the frequency division control method and they take effect on the battery and UC ports respectively, the load current ripples can be separated based on their frequencies. As shown
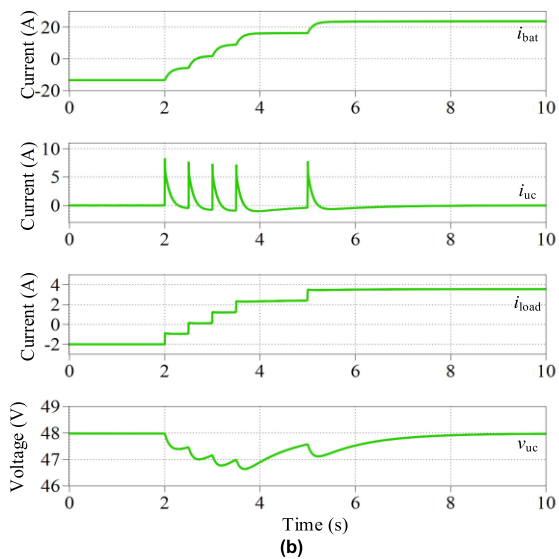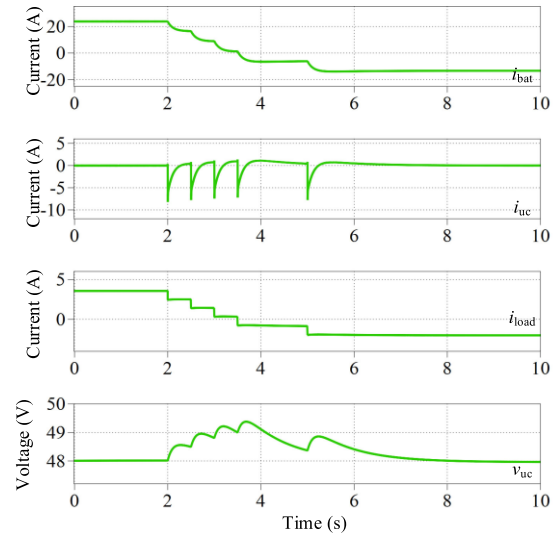

FIGURE 11. Simulation scenario #2: (a) the battery switching from discharging to charging, (b) the battery switching from charging to discharging.

in Fig. 12, when a periodical perturbation is involved at the load current, it can be seen that by using the frequency division control, the battery at port #1 majorly provides the steady-state current, i.e., the DC component of the steady-state current. On the other hand, the UC at port #2 is responsible for supplying the high-frequency ripple current. Therefore, the load current can be separated between the battery and UC ports.

V. EXERIMENTAL RESULTS
In order to validate the feasibility of the proposed control method, a HESS prototype with local load, ESUs and DC bus is set up. As shown in Fig. 13, the three ports of the TPC are connected to the battery, UC and DC bus, respectively, and a local DC load is connected to the DC bus. Two controllers based on ARM^{TM} core are employed to achieve a low-cost control framework.
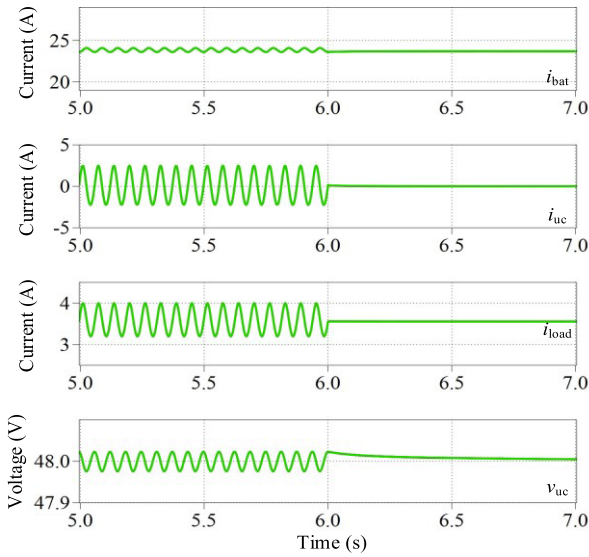
FIGURE 12. Simulation scenario #3: load power fluctuates periodically.
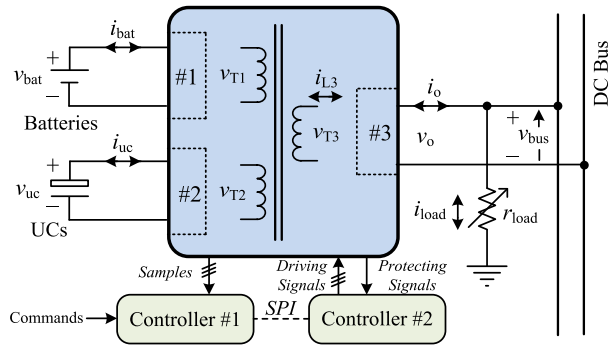

FIGURE 13. Configuration of the HESS prototype of DC MG.
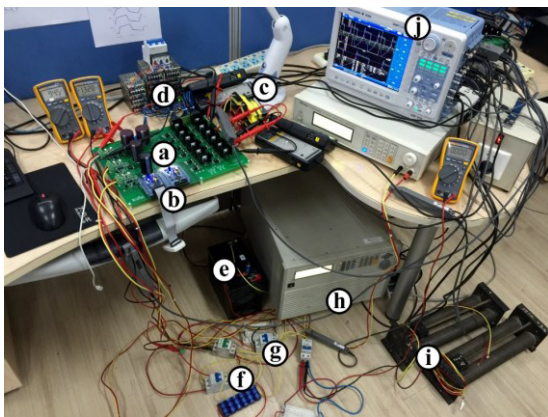

FIGURE 14. Experimental prototypes: (a) main power circuit, (b) dual-controller, (c) three-winding HFT, (d) auxiliary power supply, (e) VRLA battery, (f) UC, (g) breakers, (h) programmable electronic load, (i) resistors, (j) waveform recorder.

The configuration of the scale-down prototype is depicted in Fig. 14. The TPC is comprised of a main power circuit, a three-winding HFT, two controllers with SPI and an auxiliary power supply. A programmable DC electronic load is set at the resistance mode and it can be adjusted in the
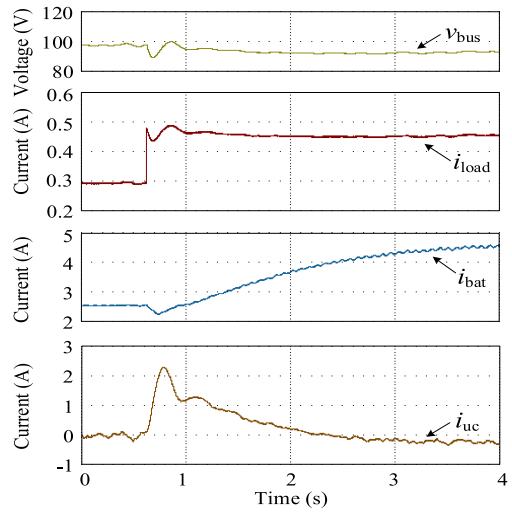

FIGURE 15. Experimental results of the proposed TPC-interfaced HESS with frequency division control: load step-up.
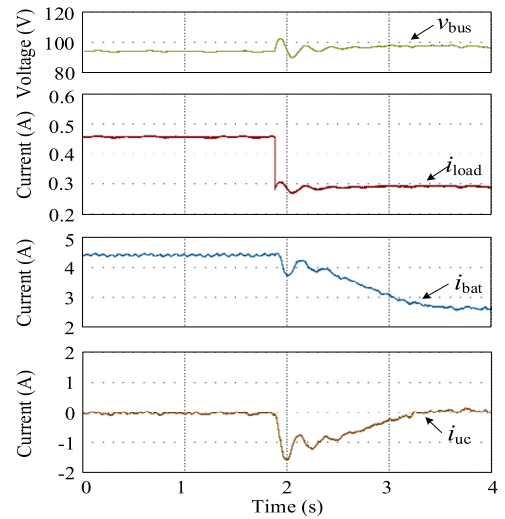

FIGURE 16. Experimental results of the proposed TPC-interfaced HESS with frequency division control: load step-down.

host computer or directly changed by using its control panel. Therefore, the step-load changes and load fluctuations conditions can be emulated by regulating the resistance of the DC electronic load.

Aiming at achieving proper power sharing of TPC-interfaced HESS in different frequency range, corresponding experimental results are shown below.

As shown in Fig. 15, when the load steps up, the load current i_{load} increases rapidly. With the proposed virtual inductance and virtual capacitance control method, the UC current i_{uc} responds to the transient step-up of the load current i_{load} immediately; then it decreases gradually to zero after the transient process. Meanwhile, the output current of the battery increases gradually and eventually becomes stable to provide steady-state load current.

Similarly, when the load steps down, as seen in Fig. 16, the UC current i_{uc} rapidly responds to the transient step-down

of the load current i_{load}, and then it gradually returns to 0. The output current of the battery i_{bat} decreases gradually and responds to the steady-state load current variation in the DC MG.
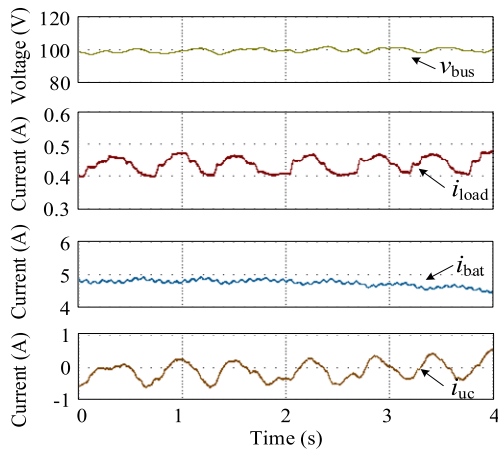

FIGURE 17. Experimental results of the proposed TPC-interfaced HESS with frequency division control: periodical load power fluctuation.

In Fig. 17, when the load current i_{load} changes periodically, the UC current i_{uc} can follow the variation and compensate the corresponding high-frequency power mismatch. On the other hand, the output current fluctuation of the battery is highly attenuated, which validates the effectiveness of the frequency division based power sharing between the battery and the UC port.

VI. CONCLUSION

In this paper, a TPC-interfaced HESS in a DC MG is proposed with autonomous frequency division based control method implemented using virtual inductance and virtual capacitance. By using a full bridge isolated TPC as the interface converter among the battery, UC and DC bus, high voltage conversion ratio, high power density and modular design can be achieved simultaneously. Simulation and experimental results validate the rational power sharing between battery and UC ports in different frequency ranges. It can be demonstrated that in the proposed system, the steady-state load current is supplied by the battery port while the transient power mismatch is compensated by the UC port. A smooth transition between charging and discharging modes of the battery is achieved by using the autonomous control method with virtual inductance and capacitance loops. Furthermore, the proposed TPC-interfaced HESS is operated relying on local measurements only, featuring the characteristics of distributed and scalable architecture.

REFERENCES

[1] J. M. Carrasco *et al.*, "Power-electronic systems for the grid integration of renewable energy sources: A survey," *IEEE Trans. Ind. Electron.*, vol. 53, no. 4, pp. 1002–1016, Jun. 2006.

[2] M. Liserre, T. Sauter, and J. Y. Hung, "Future energy systems: Integrating renewable energy sources into the smart power grid through industrial electronics," *IEEE Ind. Electron. Mag.*, vol. 4, no. 1, pp. 18–37, Mar. 2010.

[3] R. Lasseter *et al.*, "The CERTS microgrid concept. White paper on integration of distributed energy resources," U.S. Dept. Energy, Lawrence Berkeley Nat. Lab., Berkeley, CA, USA, Tech. Rep. LBNL-50829, 2002.

[4] S. Parhizi, H. Lotfi, A. Khodaei, and S. Bahramirad, "State of the art in research on microgrids: A review," *IEEE Access*, vol. 3, pp. 890–925, 2015.

[5] Y. Sun, X. Hou, J. Yang, H. Han, M. Su, and J. M. Guerrero, "New perspectives on droop control in AC microgrid," *IEEE Trans. Ind. Electron.*, vol. 64, no. 7, pp. 5741–5745, Jul. 2017.

[6] C. Dou, D. Yue, Z. Zhang, and J. M. Guerrero, "Hierarchical delay-dependent distributed coordinated control for DC ring-bus microgrids," *IEEE Access*, vol. 5, pp. 10130–10140, 2017.

[7] D. Kumar, F. Zare, and A. Ghosh, "DC microgrid technology: System architectures, AC grid interfaces, grounding schemes, power quality, communication networks, applications, and standardizations aspects," *IEEE Access*, vol. 5, pp. 12230–12256, 2017.

[8] X. Lu, J. M. Guerrero, K. Sun, and J. C. Vasquez, "An improved droop control method for DC microgrids based on low bandwidth communication with DC bus voltage restoration and enhanced current sharing accuracy," *IEEE Trans. Power Electron.*, vol. 29, no. 4, pp. 1800–1812, Apr. 2014.

[9] P. Wang, J. Xiao, and L. Setyawan, "Hierarchical control of hybrid energy storage system in DC microgrids," *IEEE Trans. Ind. Electron.*, vol. 62, no. 8, pp. 4915–4924, Aug. 2015.

[10] J. M. Guerrero, P. C. Loh, T.-L. Lee, and M. Chandorkar, "Advanced control architectures for intelligent microgrids—Part II: Power quality, energy storage, and AC/DC microgrids," *IEEE Trans. Ind. Electron.*, vol. 60, no. 4, pp. 1263–1270, Apr. 2013.

[11] P. Arboleya, C. G.-M. P. Garcia, J. Garcia, and B. Mohamed, "Hierarchical coordination of a hybrid AC/DC smartgrid with central/distributed energy storage," in *Proc. IEEE Energy Convers. Congr. Expo. (ECCE)*, Milwaukee, WI, USA, Sep. 2016, pp. 1–7.

[12] T. Morstyn, B. Hredzak, and V. G. Agelidis, "Control strategies for microgrids with distributed energy storage systems: An overview," *IEEE Trans. Smart Grid*, in press, doi: 10.1109/TSG.2016.2637958.

[13] B. Zhao, X. Zhang, J. Chen, C. Wang, and L. Guo, "Operation optimization of standalone microgrids considering lifetime characteristics of battery energy storage system," *IEEE Trans. Sustain. Energy*, vol. 4, no. 4, pp. 934–943, Oct. 2013.

[14] S. Hazra and S. Bhattacharya, "Hybrid energy storage system comprising of battery and ultra-capacitor for smoothing of oscillating wave energy," in *Proc. IEEE Energy Convers. Congr. Expo. (ECCE)*, Milwaukee, WI, USA, Sep. 2016, pp. 1–8.

[15] J. Cao and A. Emadi, "A new battery/ultracapacitor hybrid energy storage system for electric, hybrid, and plug-in hybrid electric vehicles," *IEEE Trans. Power Electron.*, vol. 27, no. 1, pp. 122–132, Jan. 2012.

[16] F. Garcia-Torres and C. Bordons, "Optimal economical schedule of hydrogen-based microgrids with hybrid storage using model predictive control," *IEEE Trans. Ind. Electron.*, vol. 62, no. 8, pp. 5195–5207, Aug. 2015.

[17] G. Xu, C. Shang, S. Fan, X. Hu, and H. Cheng, "A hierarchical energy scheduling framework of microgrids with hybrid energy storage systems," *IEEE Access*, vol. 6, pp. 2472–2483, 2018.

[18] X. Roboam, O. Langlois, H. Piquet, B. Morin, and C. Turpin, "Hybrid power generation system for aircraft electrical emergency network," *IET Elect. Syst. Transp.*, vol. 1, no. 4, pp. 148–155, 2011.

[19] C. M. Colson, M. H. Nehrir, R. K. Sharma, and B. Asghari, "Improving sustainability of hybrid energy systems—Part II: Managing multiple objectives with a multiagent system," *IEEE Trans. Sustain. Energy*, vol. 5, no. 1, pp. 46–54, Jan. 2014.

[20] H. Zhou, T. Bhattacharya, D. Tran, T. S. T. Siew, and A. M. Khambadkone, "Composite energy storage system involving battery and ultracapacitor with dynamic energy management in microgrid applications," *IEEE Trans. Power Electron.*, vol. 26, no. 3, pp. 923–930, Mar. 2011.

[21] J. Shen and A. Khaligh, "A supervisory energy management control strategy in a battery/ultracapacitor hybrid energy storage system," *IEEE Trans. Transport. Electrific.*, vol. 1, no. 3, pp. 223–231, Oct. 2015.

[22] L. Bai, F. Li, Q. Hu, H. Cui, and X. Fang, "Application of battery-supercapacitor energy storage system for smoothing wind power output: An optimal coordinated control strategy," in *Proc. IEEE Power Energy Soc. Gen. Meeting (PESGM)*, Boston, MA, USA, Jul. 2016, pp. 1–5.

[23] M. Mao, Y. Liu, P. Jin, H. Huang, and L. Chang, "Energy coordinated control of hybrid battery-supercapacitor storage system in a microgrid," in *Proc. 4th IEEE Int. Symp. Power Electron. Distrib. Generat. Syst. (PEDG)*, Rogers, AR, USA, Jul. 2013, pp. 1–6.

[24] Z. Jin, L. Meng, J. M. Guerrero, and R. Han, "Hierarchical control design for a shipboard power system with DC distribution and energy storage aboard future more-electric ships," *IEEE Trans. Ind. Informat.*, vol. 14, no. 2, pp. 703–714, Feb. 2018, doi: 10.1109/TII.2017.2772343.

[25] Z. Jin, L. Meng, J. C. Vasquez, and J. M. Guerrero, "Frequency-division power sharing and hierarchical control design for DC shipboard microgrids with hybrid energy storage systems," in *Proc. IEEE Appl. Power Electron. Conf. Expo. (APEC)*, Tampa, FL, USA, Mar. 2017, pp. 3661–3668.

[26] Y. Gu, W. Li, and X. He, "Frequency-coordinating virtual impedance for autonomous power management of DC microgrid," *IEEE Trans. Power Electron.*, vol. 30, no. 4, pp. 2328–2337, Apr. 2015.

[27] Y. Zhang and Y. W. Li, "Energy management strategy for supercapacitor in droop-controlled DC microgrid using virtual impedance," *IEEE Trans. Power Electron.*, vol. 32, no. 4, pp. 2704–2716, Apr. 2017.

[28] P. Lin, P. Wang, J. Xiao, J. Wang, C. Jin, and Y. Tang, "An integral droop for transient power allocation and output impedance shaping of hybrid energy storage system in DC microgrid," *IEEE Trans. Power Electron.*, vol. 33, no. 7, pp. 6262–6277, Jul. 2018, doi: 10.1109/TPEL.2017.2741262.

[29] Q. Xu, J. Xiao, X. Hu, P. Wang, and M. Y. Lee, "A decentralized power management strategy for hybrid energy storage system with autonomous bus voltage restoration and state-of-charge recovery," *IEEE Trans. Power Electron.*, vol. 64, no. 9, pp. 7098–7108, Sep. 2017.

[30] H. Tao, A. Kotsopoulos, J. L. Duarte, and M. A. M. Hendrix, "Family of multiport bidirectional DC-DC converters," *IEE Proc.-Electr. Power Appl.*, vol. 153, no. 3, pp. 451–458, May 2006.

[31] H. Wu, P. Xu, H. Hu, Z. Zhou, and Y. Xing, "Multiport converters based on integration of full-bridge and bidirectional DC–DC topologies for renewable generation systems," *IEEE Trans. Power Electron.*, vol. 61, no. 2, pp. 856–869, Feb. 2014.

[32] S. J. Al-Chlaihawi and A. G. Al-Gizi, "A survey of multiport converters used in renewable energy," in *Proc. Int. Symp. Fundam. Electr. Eng. (ISFEE)*, Bucharest, Romania, Jun./Jul. 2016, pp. 1–4.

[33] H. Wu, J. Zhang, and Y. Xing, "A family of multiport buck–boost converters based on DC-link-inductors (DLIs)," *IEEE Trans. Power Electron.*, vol. 30, no. 2, pp. 735–746, Feb. 2015.

[34] H. Tao, J. L. Duarte, and M. A. M. Hendrix, "Multiport converters for hybrid power sources," in *Proc. IEEE Power Electron. Spec. Conf.*, Rhodes, Greece, Jun. 2008, pp. 3412–3418.

[35] S. Inoue and H. Akagi, "A bidirectional DC–DC converter for an energy storage system with galvanic isolation," *IEEE Trans. Power Electron.*, vol. 22, no. 6, pp. 2299–2306, Nov. 2007.

[36] Z. Wang and H. Li, "An integrated three-port bidirectional DC–DC converter for PV application on a DC distribution system," *IEEE Trans. Power Electron.*, vol. 28, no. 10, pp. 4612–4624, Oct. 2013.

[37] C. Zhao, S. D. Round, and J. W. Kolar, "An isolated three-port bidirectional DC-DC converter with decoupled power flow management," *IEEE Trans. Power Electron.*, vol. 23, no. 5, pp. 2443–2453, Sep. 2008.

PANBAO WANG (S'10–M'11) received the M.S. and Ph.D. degrees in electrical engineering from Harbin Institute of Technology, China, in 2011 and 2016, respectively. In 2017, he joined the Department of Electrical Engineering, Harbin Institute of Technology, where he is currently a Lecturer.

His research interests include DC microgrid system model analysis, operation and control, power electronics converters for hybrid storage system, and optimal control in multi-microgrids.
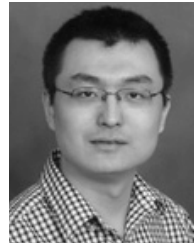
XIAONAN LU (S'12–M'13) received the B.E. and Ph.D. degrees in electrical engineering from Tsinghua University, Beijing, China, in 2008 and 2013, respectively. He was also a transfer Ph.D. at Aalborg University from 2010 to 2011. In 2015, he joined the Energy Systems Division, Argonne National Laboratory, where he is currently an Energy Systems Scientist.

His research interests include modeling and control of power electronic converters in ac and dc microgrids, hardware-in-the-loop real-time simulation, and distribution automation. He received the Outstanding Reviewer Award for IEEE Transactions on Power Electronics in 2013, the Outstanding Reviewer Award for IEEE Transactions on Smart Grid in 2015, and the Outstanding Postdoctoral Performance Award at Argonne National Laboratory in 2016.

Dr. Lu is a member of the IEEE Power Electronics Society, the Industry Applications Society, the Power and Energy Society, and the Industrial Electronics Society. He was also elected as the Secretary of the Industrial Power Converter Committee in the IEEE IAS. He is an Editor of IEEE Transactions on Smart Grid and an Associate Editor of IEEE Transactions on Industry Applications.

WEI WANG (M'13) received the B.S. degree in automatic test and control, the M.S. degree in electrical engineering, and the Ph.D. degree in mechanical electronic engineering from Harbin Institute of Technology, Harbin, China, in 1984, 1990, and 2002, respectively. Since 2003, she has been a Professor with the Department of Electrical Engineering, Harbin Institute of Technology.

She is involved in research on soft-switching converters, photovoltaic grid-connected inverters, and ac and dc microgrids.

DIANGUO XU (M'97–SM'12–F'17) received the B.S. degree in control engineering from Harbin Engineering University, Harbin, China, in 1982, and the M.S. and Ph.D. degrees in electrical engineering from the Harbin Institute of Technology (HIT), Harbin, in 1984 and 1989, respectively.

In 1984, he joined the Department of Electrical Engineering, HIT, as an Assistant Professor, where he has been a Professor since 1994. He was the Dean of the School of Electrical Engineering and Automation, HIT, from 2000 to 2010. He is currently the Vice President of HIT. He has published over 1000 technical papers. His research interests include renewable energy generation technology, multi-terminal high-voltage direct current system based on voltage-source converter, power quality mitigation, speed sensor-less vector controlled motor drives, and a high-performance permanent magnet synchronous motor servo system.

Dr. Xu serves as the Chairman for the IEEE Harbin Section, the Director for the Lighting Power Supply Committee of CPSS, and the Vice-Director for the Electric Automation Committee of CAA, the Electrical Control System and Equipment Committee of CES, and the Power Electronics Committee of CES. He is also an Associate Editor of IEEE Transactions on Industrial Electronics and IEEE Journal of Emerging and Selected Topics in Power Electronics.

• • •